Inorganic Chemistry

Article

pubs.acs.org/IC

Importance of Halogen···Halogen Contacts for the Structural and Magnetic Properties of CuX_2(pyrazine-*N*,*N*′-dioxide)$(H_2O)_2$ (X = Cl and Br)

John A. Schlueter,*[,†] Hyunsoo Park,[†] Gregory J. Halder,[†,‡] William R. Armand,[†] Cortney Dunmars,[†] Karena W. Chapman,[‡] Jamie L. Manson,[§] John Singleton,[⊥] Ross McDonald,[⊥] Alex Plonczak,[⊥] Jinhee Kang,[∥] Chaghoon Lee,[∥] Myung-Hwan Whangbo,[∥] Tom Lancaster,[#,▽] Andrew J. Steele,[#] Isabel Franke,[#] Jack D. Wright,[#] Stephen J. Blundell,[#] Francis L. Pratt,[&] Joseph deGeorge,[@] Mark M. Turnbull,[@] and Christopher P. Landee[@]

[†]Materials Science Division, Argonne National Laboratory, Argonne, Illinois 60439, United States

[‡]X-ray Science Division, Advanced Photon Source, Argonne National Laboratory, Argonne, Illinois 60439, United States

[§]Department of Chemistry and Biochemistry, Eastern Washington University, Cheney, Washington 99004, United States

[⊥]National High Magnetic Field Laboratory, Los Alamos National Laboratory, Los Alamos, New Mexico 87545, United States

[∥]Department of Chemistry, North Carolina State University, Raleigh, North Carolina 27695-8204, United States

[#]Department of Physics, Clarendon Laboratory, Oxford University, Parks Road, Oxford, OX1 3PU, United Kingdom

[&]ISIS Facility, Rutherford Appleton Laboratory, Chilton, Oxfordshire OX11 0QX, United Kingdom

[@]Carlson School of Chemistry and Department of Physics, Clark University, Worcester, Massachusetts 01610, United States

Supporting Information

ABSTRACT: The structural and magnetic properties of the newly crystallized $CuX_2(pyzO)(H_2O)_2$ (X = Cl, Br; pyzO = pyrazine-*N*,*N*′-dioxide) coordination polymers are reported. These isostructural compounds crystallize in the monoclinic space group $C2/c$ with, at 150 K, a = 17.0515(7) Å, b = 5.5560(2) Å, c = 10.4254(5) Å, β = 115.400(2)°, and V = 892.21(7) Å^3 for X = Cl and a = 17.3457(8) Å, b = 5.6766(3) Å, c = 10.6979(5) Å, β = 115.593(2)°, and V = 950.01(8) Å^3 for X = Br. Their crystal structure is characterized by one-dimensional chains of Cu^{2+} ions linked through bidentate pyzO ligands. These chains are joined together through OH···O hydrogen bonds between the water ligands and pyzO oxygen atoms and Cu−X···X−Cu contacts. Bulk magnetic susceptibility measurements at ambient pressure show a broad maximum at 7 (Cl) and 28 K (Br) that is indicative of short-range magnetic correlations. The dominant spin exchange is the Cu−X···X−Cu supersuperexchange because the magnetic orbital of the Cu^{2+} ion is contained in the $CuX_2(H_2O)_2$ plane and the X···X contact distances are short. The magnetic data were fitted to a Heisenberg 1D uniform antiferromagnetic chain model with J_{1D}/k_B = −11.1(1) (Cl) and −45.9(1) K (Br). Magnetization saturates at fields of 16.1(3) (Cl) and 66.7(5) T (Br), from which J_{1D} is determined to be −11.5(2) (Cl) and −46.4(5) K (Br). For the Br analog the pressure dependence of the magnetic susceptibility indicates a gradual increase in the magnitude of J_{1D}/k_B up to −51.2 K at 0.84 GPa, suggesting a shortening of the Br···Br contact distance under pressure. At higher pressure X-ray powder diffraction data indicates a structural phase transition at ∼3.5 GPa. Muon-spin relaxation measurements indicate that $CuCl_2(pyzO)(H_2O)_2$ is magnetically ordered with T_N = 1.06(1) K, while the signature for long-range magnetic order in $CuBr_2(pyzO)(H_2O)_2$ was much less definitive down to 0.26 K. The results for the $CuX_2(pyzO)(H_2O)_2$ complexes are compared to the related CuX_2(pyrazine) materials.

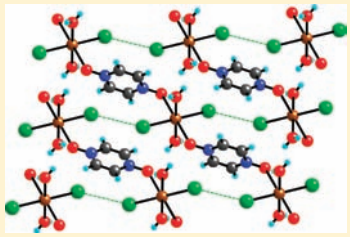

INTRODUCTION

The importance of intermolecular halogen···halogen contacts in molecular systems has been increasingly studied in recent years. These intermolecular interactions are important for the design of functional materials and play critical roles in conducting and magnetic systems.[1,2] Recently, a strong antiferromagnetic coupling of −234 K was found for the Cu−Br···Br−Cu supersuperexchange in Cu(2,5-dimethylpyrazine)Br_2.[3]

The crystal structures of CuX_2(pyz) (pyz = pyrazine; X = Cl[4] or Br[5]) consist of Cu−X_2−Cu bibridged chains that are linked through bridging pyrazine molecules resulting in a two-dimensional (2D) rectangular lattice. Each Cu^{2+} ion is coordinated by two long and two short Cu−X bonds. Three-dimensional (3D) antiferromagnetic order was discovered in these coordination polymers at 3.6 (Br) and 3.2 K (Cl) through the use of muon-spin relaxation.[6] Monte Carlo simulations have been used to determine the spin exchanges J = −23(1) K and J' = −5(1) K for X = Br and J = −14(1) K and J' = −4(1) K for X = Cl.[7]

Received: September 1, 2011
Published: February 1, 2012

   dx.doi.org/10.1021/ic201924q | *Inorg. Chem.* 2012, 51, 2121−2129

Whereas pyz has been used extensively as a bridging ligand in coordination polymers, pyrazine-*N*,*N*′-dioxide (pyzO) has received much less attention. Recent magnetic studies of $Mn(N_3)_2(pyzO)$[8] and $M(NCS)_2(pyzO)_2$ (M = Mn, Co)[9] indicate that pyzO has the potential to mediate significant spin exchanges. In the case of $Co[N(CN)_2]_2(pyzO)$, the pyzO ligands link triangular $Co[N(CN)_2]_2$ layers into a 3D motif with long-range magnetic ordering below 2.5 K.[10] The oxophilic nature of lanthanide ions has allowed the preparation of a series of 3D networks with luminescence properties.[11] $Cu_2(ClO_4)_4(pyzO)_3(H_2O)_2$ is the only structurally characterized example of a pyzO coordination polymer with Cu^{2+}.[12] $CoBr_2(pyzO)(H_2O)_2$ contains zigzag Co−pyzO−Co chains with cis coordination about the Co^{2+} ion.[12] The magnetic properties of these latter two materials have not been reported yet.

Molecular materials are often referred to as 'soft' because of their frequently large compressibilities. Although still relatively sparse in the literature, magnetic properties of coordination polymers as a function of pressure have been increasingly studied during recent years.[13−21] In general, magnetic ordering temperatures increase with applied pressure as a result of increased overlap between magnetic orbitals. Due to their highly anisotropic structural features, one might anticipate anisotropic compressibilities and pressure-induced phase transitions from them. Structure−property relationships as a function of pressure are rarely reported for these systems but must be understood to accurately describe magnetic coupling.

The pyzO ligand is a promising molecular building block for formation of coordination polymers that have the potential to mediate spin exchange. We have chosen to study this bidentate ligand as a component of relatively simple coordination polymers where fundamental structure−property relationships as a function of pressure can be established. Specifically, we have chosen to investigate the copper(II) halide coordination polymers of pyzO as the halogen-bonding interactions provide structure-directing entities and possible Cu−X···X−Cu super-superexchange pathways for significant magnetic coupling. Herein, we describe the crystallization of the $CuX_2(pyzO)(H_2O)_2$ (X = Cl, Br) coordination polymers and present a detailed study of their crystal and magnetic structures through use of state-of-the-art techniques including X-ray powder diffraction and SQUID magnetometry at ambient and elevated pressure, pulsed field magnetization to fields of 90 T, muon-spin relaxation studies, and density functional calculations.

EXPERIMENTAL SECTION

All chemical reagents were of analytical grade and used without further purification. Elemental analyses were performed by Midwest Microlab (Indianapolis, IN).

Synthesis of $CuCl_2(pyzO)(H_2O)_2$ (1) and $CuBr_2(pyzO)(H_2O)_2$ (2). PyzO (2 mmol, 0.2242 g, Alfa) was dissolved in hot distilled water (10 mL). An aqueous solution (5 mL) of $CuCl_2{\cdot}2.5H_2O$ (1 mmol, 0.1795 g, Aldrich) was then added dropwise to pyzO solution. Green, needle-like single crystals of **1** were obtained by slow evaporation of water at room temperature over a period of 1 week. Anal. Calcd for $C_4H_8Cl_2CuN_2O_4$: C, 17.00; H, 2.85; Cl, 25.09; N, 9.91. Found: C, 16.95; H, 2.77; Cl, 25.30; N, 9.83. IR (cm^{-1}): 3121 w, 3055 m, 3021 m, 2988 w, 1481 m, 1461 s, 1227 s, 1059 m, 869 m, 799 s. To obtain **2**, the above procedure was applied, substituting $CuCl_2$ with $CuBr_2$ (1 mmol, 0.2224 g). Large green needles were recovered upon evaporation of water at room temperature. Anal. Calcd for $C_4H_8Br_2CuN_2O_4$: C, 12.93; H, 2.17; Br, 43.02; N, 7.54. Found: C, 13.25; H, 2.15; Br, 42.95; N, 7.52. IR (cm^{-1}): 3121 w, 3055 w, 3025 m, 2986 w, 1479 m, 1456 s, 1226 s, 1060 m, 860 m, 799 s.

Synthesis of $CuCl_2(Pyz)$ (3) and $CuBr_2(Pyz)$ (4). Pyrazine (2 mmol, 0.160 g, Aldrich) was dissolved in distilled water (10 mL). An aqueous solution (5 mL) of $CuCl_2{\cdot}2.5H_2O$ (1 mmol, 0.1795 g, Aldrich) was then added dropwise to the pyz solution. Brown, blocky crystals of **3** were obtained by slow evaporation of water at room temperature over a period of 1 week. Anal. Calcd for $C_4H_4Cl_2CuN_2$: C, 22.39; H, 1.88; Cl, 33.05; N, 13.06. Found: C, 22.59; H, 2.06; Cl, 32.91; N, 12.89. IR (cm^{-1}): 3117 w, 3111 w, 1482 w, 1413 s, 1281 m, 1165 s, 1113 s, 1092 m, 1065 s, 866 w, 802 vs. To obtain **4**, the above procedure was applied, substituting $CuCl_2$ with $CuBr_2$ (1 mmol, 0.2224 g). Green blocky crystals were recovered upon evaporation of water at room temperature. Anal. Calcd for $C_4H_4Br_2CuN_2$: C, 15.83; H, 1.33; Br, 52.66; N, 9.23. Found: C, 15.89; H, 1.35; Br, 52.78; N, 9.25. IR (cm^{-1}): 3111 w, 3102 w, 3055 w, 1483 m, 1412 vs, 1362 w, 1279 m, 1161 s, 1113 s, 1092 m, 1062 s, 966 w, 868 w, 796 vs.

Thermogravimetric Analysis (TGA). Data were collected on a TA Instruments Q50 thermogravimetric analyzer in flowing nitrogen at a heating rate of 10 °C/min to a final temperature of 500 °C.

Infrared Spectroscopy. Infrared spectra were measured between 4000 and 750 cm^{-1} through use of a Bruker Vertex 70 spectrometer equipped with a PIKE Technologies MIRacle attenuated total reflectance (ATR) stage.

Single-Crystal X-ray Diffraction. Green needles of **1** and **2** with dimensions of 0.45 × 0.15 × 0.10 and 0.40 × 0.10 × 0.10 mm^3, respectively, were placed onto the tip of a glass fiber and mounted on a Bruker APEX II 3-circle diffractometer equipped with an APEX II detector at 150(2) K. Data collection was carried out using Mo Kα radiation (λ = 0.71073 Å) with a frame exposure time of 30 s and a detector distance of 5.00 cm. Five major sections of frames were collected with 0.50° ϕ and ω scans. Data to a resolution of 0.68 Å were considered in the reduction. The raw intensity data were corrected for absorption (SADABS[22]). The structure was solved and refined using SHELXTL.[23] A direct-method solution was calculated, which provided most of the atomic positions from the E map. Full-matrix least-squares/difference Fourier cycles were performed, which located the remaining atoms. All non-hydrogen atoms were refined with anisotropic displacement parameters. Hydrogen atoms from the water molecule were located from difference Fourier map. All other hydrogen atoms were placed in ideal positions and refined as riding atoms with relative isotropic displacement parameters. Structural and refinement parameters are provided in Table 1.

Table 1. Crystal Data and Structure Refinement of Complexes 1 and 2[a]

	1	2
formula	$C_4H_8Cl_2CuN_2O_4$	$C_4H_8Br_2CuN_2O_4$
M_W	282.57	371.48
cryst syst	monoclinic	monoclinic
T/K	150(2)	150(2)
wavelength	0.71073 Å	0.71073 Å
space group	$C2/c$	$C2/c$
a/Å	17.0515(7)	17.3457(8)
b/Å	5.5560(2)	5.6766(3)
c/Å	10.4254(5)	10.6979(5)
β/°	115.400(2)	115.593(2)
V/Å^3	892.21(7)	950.01(8)
Z	4	4
ρ/g/cm^{-3}	2.104	2.597
μ/mm^{-1}	3.029	10.695
F(000)	564	708
GoF	1.058	1.062
R, R_w [$I > 2\sigma(I)$]	0.0221, 0.0589	0.0292, 0.0727
R, R_w (all data)	0.0223, 0.0590	0.0304, 0.0734

[a] $R1 = \Sigma||F_o| - |F_c||/\Sigma|F_o|$; $wR2 = [\Sigma w(F_o^2 - F_c^2)^2/\Sigma w(F_o^2)^2]^{1/2}$; GoF = $[\Sigma w(F_o^2 - F_c^2)^2/(N_d - N_p)]^{1/2}$; $R_{int} = \Sigma|F_o^2 - F_o^2(\text{mean})|/\Sigma wF_o^2$.

dx.doi.org/10.1021/ic201924q | Inorg. Chem. 2012, 51, 2121−2129

Powder X-ray Diffraction under Pressure. The pressure-dependent structures of **2** and **4** were probed using synchrotron-based powder diffraction for samples within a diamond anvil cell pressure apparatus. In-situ X-ray diffraction data (λ = 0.6051 Å) were collected at the 1-BM beamline at the Advanced Photon Source, Argonne National Laboratory at ~30 pressures in the range 0−6 GPa. Polycrystalline NaCl was included as an internal pressure marker, and isopropanol was used to mediate hydrostatic compression. For each diffraction pattern, lattice parameters were refined via the Le Bail profile-fitting method[24] through the use of FullProf.[25]

Magnetic Measurements. Variable-temperature dc magnetic susceptibility and field dependence of magnetization were performed on a Quantum Design MPMS-7XL SQUID magnetometer equipped with a 70 000 Oe superconducting magnet and reciprocating sample option. Homogeneous powder samples were loaded into gelatin capsules and mounted on the end of a carbon fiber rod. The samples were cooled in zero field to the lowest achievable temperature of 2 K, the magnet charged to 1000 Oe, and data collected on warming to 300 K. Experimental susceptibilities were corrected for the diamagnetism of the constituent atoms.

Pressure-dependent magnetic susceptibility data were collected using a piston-based pressure cell (MCell-10, EasyLab Industries, P_{max} = 1.2 GPa). Polycrystalline **2** or **4** was loaded in the cell with silicon oil pressure-transmitting fluid and a Sn pressure standard. Variable-temperature data were collected at pressures up to ~1 GPa.

Pulsed-Field Magnetization. Pulsed-field magnetization experiments of polycrystals of **1**−**4** used a 1.5 mm bore, 1.5 mm long, 1500-turn compensated-coil susceptometer, constructed from 50-gauge high-purity copper wire.[26] When a sample is within the coil, the signal voltage V is proportional to (dM/dt), where t is the time. Numerical integration of V is used to evaluate M. The sample is mounted within a 1.3 mm diameter ampule that can be moved in and out of the coil.[26] Accurate values of M are obtained by subtracting empty coil data from that measured under identical conditions with the sample present.[26] Fields were provided by a 60 T short-pulse magnet or by the 100 T multishot magnet at NHMFL Los Alamos. The susceptometer was placed within a ^{3}He cryostat, providing temperatures down to 0.4 K. The field B was measured by integrating the voltage induced in a 10-turn coil calibrated by observing the de Haas−van Alphen oscillations of the belly orbits of the copper coils of the susceptometer.[26]

Muon-Spin Relaxation. Zero-field (ZF) muon-spin relaxation (μ^+SR) measurements were made at the ISIS facility, Rutherford Appleton Laboratory, U.K., using the ARGUS instrument. Powder samples were packed in 12.5 μm Ag foil packets and mounted on the Ag coldfinger of a ^{3}He cryostat.

In a μ^+SR experiment[27] spin-polarized positive muons are stopped in a target sample, where the muon usually occupies an interstitial position in the crystal. The observed property in the experiment is the time evolution of the muon-spin polarization, the behavior of which depends on the local magnetic field at the muon site. Each muon decays, with an average lifetime of 2.2 μs, into two neutrinos and a positron, the latter particle being emitted preferentially along the instantaneous direction of the muon spin. Recording the time dependence of the positron emission directions therefore allows determination of the spin polarization of the ensemble of muons. In our experiments positrons are detected by detectors placed forward (F) and backward (B) of the initial muon polarization direction. Histograms $N_F(t)$ and $N_B(t)$ record the number of positrons detected in the two detectors as a function of time following muon implantation. The quantity of interest is the decay positron asymmetry function, defined as

$$A(t) = \frac{N_F(t) - \alpha_{exp} N_B(t)}{N_F(t) + \alpha_{exp} N_B(t)} \quad (1)$$

where α_{exp} is an experimental calibration constant. $A(t)$ is proportional to the spin polarization of the muon ensemble.

Density Functional Calculations. In order to assess the strength of the spin exchange through the Cu−X···X−Cu path in **1** and **2**, we evaluate the spin exchange interactions by performing mapping analysis based on density functional calculations. Our spin-polarized density functional calculations employed the projector-augmented wave method implemented in the Vienna ab initio simulation package[28−30] with the generalized gradient approximation (GGA)[31] for the exchange-correlation functional, the plane-wave cutoff energy of 400 eV, a set of 16 k points for the irreducible Brillouin zone, and the threshold 10^{-6} eV for energy convergence. To examine the possible effect of the electron correlation associated with Cu 3d states, we carried out GGA plus on-site repulsion U (GGA+U) calculations[32] with the effective U = 4 and 6 eV on the Cu atoms.

RESULTS AND DISCUSSION

Structure Description. Compounds **1** and **2** are isomorphous and crystallize in the monoclinic space group of $C2/c$. An ORTEP diagram of **2** is shown in Figure 1. The asymmetric unit consists of one crystallographically independent Cu site which is located on the inversion center (Wyckoff position 4c). All other atoms lie on the general positions. In the structures of both **1** and **2** the Cu^{2+} ion displays a Jahn−Teller elongation with the axial bonds to the oxygen atoms of the pyzO (Cu−O1 = 2.5647(9) and 2.6826(15) Å for **1** and **2**, respectively). The distorted octahedral geometry around Cu is completed by two *trans*-water molecules and two halide ions. The Cu−O[12] and Cu−X[4,5] bond lengths (Table 2) are similar to those previously reported. The NO bond length of the pyzO ligand is slightly longer in the coordination complexes **1** and **2** than in its uncoordinated form,[33,34] due to a decrease of the

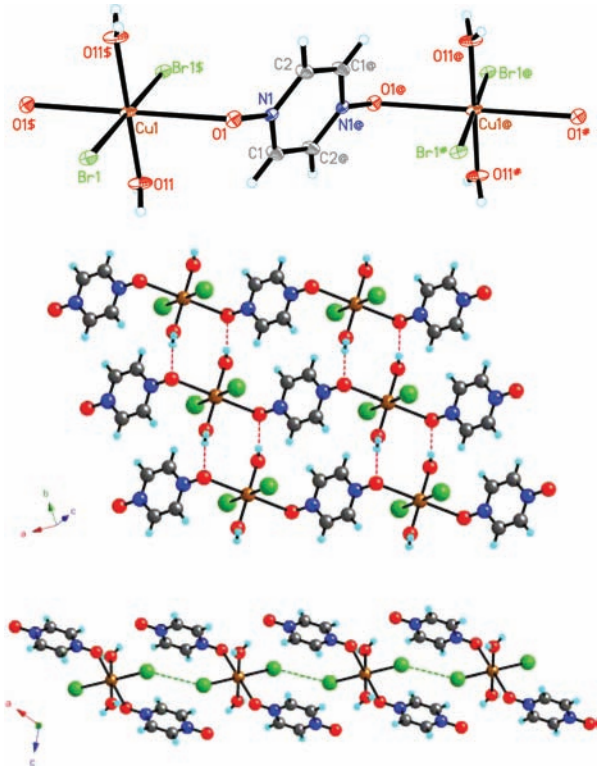

Figure 1. Depiction of the crystal structure of **2**. (Top) ORTEP diagram with thermal ellipsoids drawn at the 50% probability level. Symmetry transformations used to generate equivalent atoms are as follows: $ = −x + 1/2, −y + 1/2, −z; @ = −x, −y, −z; # = x − 1/2, y − 1/2, z. (Center) Packing diagram illustrating the hydrogen bonds linking the −Cu−pyz−Cu− chains into layers are illustrated as dashed red lines. (Bottom) Halogen contacts along the c axis link these planes into a 3D structure.

dx.doi.org/10.1021/ic201924q | Inorg. Chem. 2012, 51, 2121−2129

Table 2. Selected Bond Distances and Angles for 1 and 2

1		2	
bond distances (Å)			
Cu1−O1	2.5647(9)	Cu1−O1	2.6826(15)
Cu1−Cl1	2.2630(3)	Cu1−Br1	2.3792(2)
Cu1−O11	1.9545(10)	Cu1−O11	1.9641(14)
O1−N1	1.3174(13)	O1−N1	1.319(2)
bond angles (deg)			
O11−Cu1−Cl1	90.01(3)	O11−Cu1−Br1	90.35(5)
O11−Cu1−O1	87.24(4)	O11−Cu1−O1	87.29(6)
Cl1−Cu1−O1	89.34(2)	Br1−Cu1−O1	89.09(3)
hydrogen bonds			
O11−H11A···O1	1.950 Å, 167.38°	O11−H11A···O1	2.009 Å, 170.80°
O11−H11B···O1	1.932 Å, 175.30°	O11−H11B···O1	2.023 Å, 174.63°
C2−H2···Cl1	2.545 Å, 171.92°	C2−H2···Br1	2.629 Å, 171.68°
halogen bonds			
Cu1−Cl1···Cl1	3.7334(6) Å, 148.67(1)°	Cu1−Br1···Br1	3.6347(4) Å, 148.74(1)°

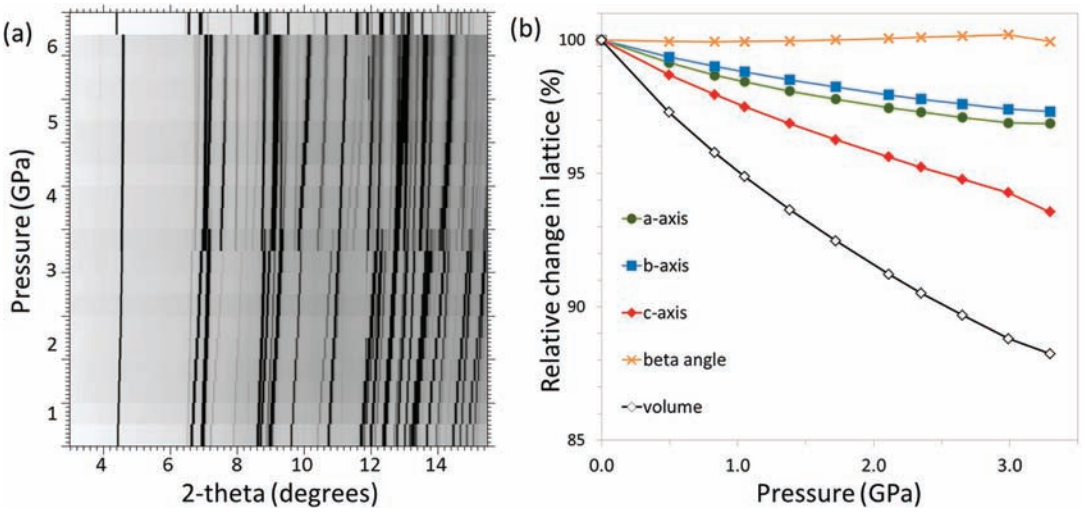

Figure 2. (Left) X-ray powder diffraction data as a function of pressure for **2**. A clear structural phase transition is evident near 4 GPa. Final scan (top of figure) was taken after the sample was returned to ambient pressure at the conclusion of the experiment. (Right) Unit cell parameters as a function of pressure.

N═O double-bond character upon coordination. The bond valence sums[35,36] around Cu are calculated to be 2.11 and 1.76 for **1** and **2**, respectively, suggesting that all bonds around Cu are correctly assigned.

The extended structures of **1** and **2** feature one-dimensional (1D) chains of Cu^{2+} ions linked through bidentate pyzO ligands. The chains at $z = 0$ run along the 110 direction, while those at $z = 0.5$ run along $1\bar{1}0$. In comparison to the intrachain Cu···Cu distances of 8.9669(3) and 9.1255(4) Å for **1** and **2**, respectively, the shortest interchain distances between two Cu centers are 5.5560(2) and 5.6766(3) Å. These chains are linked together through OH···O hydrogen bonds between the water ligands and the pyzO oxygen atoms (Table 2). Additional weak hydrogen bonds are present between the halide ions and hydrogen atoms of pyzO. As illustrated in Figure 1, the Cu−pyzO−Cu chains are further linked through Cu−X···X−Cu contacts, resulting in Cu···Cu separations of 7.8572(3) and 7.9844(4) Å for **1** and **2**, respectively.

As illustrated in Supporting Information Figure S1, the crystal structures of **1** and **2** are quite different from that of **3** and **4** in spite of the similar composition.[4,5] The crystal structures of **3** and **4** are characterized by 1D $(-Cu-pyz-)_\infty$ chains that are linked into a rectangular lattice through bibridged Cu−X···Cu interactions. Within these 2D sheets, the shortest Br···Br distances are 3.864 Å, while between sheets, the shortest Br···Br distances are 4.184 Å.

The X-ray powder diffraction patterns of **2** and **4** were determined as a function of pressure. For both materials the lattice volume shows a gradual contraction with increasing pressure (Figure 2 and Supporting Information Figure S2). The bulk moduli for **2** and **4** were found be the same within experimental error, with respective values of 16.0(16) and 16.5(11) GPa (Supporting Information Table S1), and are comparable to the reported value of 12.1(6) GPa for $Cu(pyz)(H_2O)_2F_2$.[37] In the case of **2**, the direction along the hydrogen-bonded chains (c axis) exhibits the largest relative compression with $c/c_0 = 0.94$ at 3.30 GPa, corresponding to an absolute contraction of 0.70 Å over this pressure range. For **2**, a clear phase transition is observed near 3.5 GPa, but the structure of this high-pressure phase has not been determined (Figure 2). For **4**, the direction of the $-Cu-Br_2-Cu-$ chains (c axis) shows the largest relative compression, with $c/c_0 = 0.91$ at 5.94 GPa and a net contraction of 0.35 Å over this pressure range. As compared to **2**, a larger increase in the monoclinic

dx.doi.org/10.1021/ic201924q | Inorg. Chem. 2012, 51, 2121−2129

beta angle is observed for **4** with β increasing by 0.3° and 1.7° for **2** and **4**, respectively. No structural phase transitions were observed for **4** up to ~6 GPa (Supporting Information Figure S2a). In both **2** and **4** the pressure-induced structural perturbations are completely reversible upon release of pressure.

Thermogravimetric Analysis. As illustrated in Supporting Information Figure S7, thermogravimetric analysis of **1** and **2** clearly shows the loss of coordinated water at 100 and 83 °C, respectively. The slightly higher temperature required for liberation of water in the case of **1** is likely due to stronger hydrogen bonds to the pyzO ligand, as evidenced by the shorter H···O distances (see Table 2). Catastrophic lattice decomposition via loss of the pyzO ligand occurs at 225 and 205 °C. In contrast, compounds **3** and **4** display a single-step thermal decomposition at temperatures of 265 and 225 °C, respectively, presumably due to loss of the pyr ligand. In both the $CuX_2(pyzO)(H_2O)_2$ and the $CuX_2(pyz)$ families the chloride adduct decomposes at a higher temperature that the bromide analog.

Infrared Analysis. The infrared spectra of **1** and **2** are compared to pyzO in Supporting Information Figure S8. PyzO exhibits strong N−O absorptions at 1258 and 870 cm^{-1}.[38,39] As discussed for the case of pyridine *N*-oxide,[40,41] metal coordination of such ligands result in a decrease of the NO double-bond character and a lowering of the ν(N−O) frequencies. Coordination of the *N*-oxides of aromatic azines typically results in a red shift of these vibrational frequencies.[42,43] This is clearly the case for the 1258 cm^{-1} mode that shifts to 1227 and 1226 cm^{-1} for **1** and **2**, respectively.

Evaluation of the Cu−X···X−Cu Spin Exchanges in 1 and 2. Each $CuX_2(pyzO)(H_2O)_2$ octahedron is axially elongated such that the long axial Cu−O bonds are formed with the pyzO ligands [i.e., Cu−Br = 2.379 Å, Cu−O (H_2O) = 1.964 Å, Cu−O (pyzO) = 2.683 Å in **2**, and Cu−Cl = 2.263 Å, Cu−O (H_2O) = 1.954 Å, Cu−O (pyzO) = 2.565 Å in **1**]. The magnetic orbital of the Cu^{2+} ion, commonly referred to as the "$x^2 - y^2$" orbital,[44] is contained in the $CuX_2(H_2O)_2$ "square plane". In this magnetic orbital the Cu "$x^2 - y^2$" orbital makes σ-antibonding interactions with the O 2p orbitals of the two H_2O molecules and the X *n*p (i.e., Br 4p and Cl 3p) orbitals of the two halides (Figure 3). In the crystal structures of **1** and **2** the $CuX_2(H_2O)_2$ square planes are arranged such that the magnetic orbitals of the Cu^{2+} ions can overlap substantially only through the Cu−X···X−Cu paths (Figure 1). This suggests that, to a first approximation, the magnetic properties of **1** and **2** can be described by a Heisenberg 1D uniform antiferromagnetic chain. To verify this suggestion, we evaluate the spin exchange Cu−X···X−Cu exchange J_1 plus three other exchanges (J_2−J_4 defined in Supporting Information Figure S3). To determine the values of these exchanges, we considered five ordered spin states of $CuX_2(pyzO)(H_2O)_2$ and determine their relative energies by performing GGA+U calculations (see Supporting Information Figure S4). In terms of the spin Hamiltonian

$$\hat{H} = -\sum_{i<j} J_{ij}\hat{S}_i\cdot\hat{S}_j \qquad (2)$$

where $J_{ij} = J_1$−J_4, the total spin exchange energies of the five ordered spin states are written as summarized in Supporting Information Figure S4. Thus, by mapping the relative energies of the five ordered spin states determined from the GGA+U calculations onto the corresponding relative energies determined from the spin Hamiltonian, we obtain the values of J_1−J_4 summarized in Supporting Information Table S2. As anticipated, J_1 is the strongest spin exchange and other exchanges are negligibly small, so that the magnetic properties of **1** and **2** should be described by a Heisenberg uniform antiferromagnetic chain model. Our GGA+U calculations show that $J_1/k_B = -184$ and −47 K for **2** and **1**, respectively, with U = 4 eV, while $J_1/k_B = -127$ and −31 K for **2** and **1**, respectively, with U = 6 eV. The true J_1 values should be smaller in magnitude because spin exchanges obtained by GGA+U calculations are typically overestimated by a factor of ~4.[45−47,57] However, the relative values of spin exchanges are well described by GGA+U calculations. It is interesting that J_1 is stronger for **2** than for **1** by a factor of ~4. The strength of a Cu−X···X−Cu spin exchange increases with increasing ∠Cu−X···X angle and decreasing X···X distance.[44,48] The ∠Cu−Br···Br angle of **2** is the same as the ∠Cu−Cl···Cl angle of **1** (i.e., 148.7°), but the Br···Br distance of **2** is shorter than the Cl···Cl distance of **1** (i.e., 3.635 vs 3.733 Å) so that J_1 is stronger in **2** than in **1**.

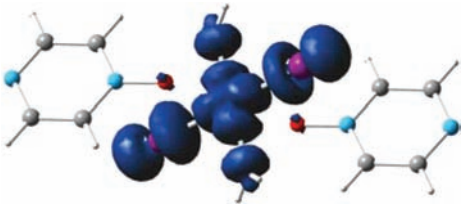

Figure 3. Spin density calculated for an isolated $CuX_2(pyzO)(H_2O)_2$, showing that the magnetic orbital of the Cu^{2+} ion lies in the $CuX_2(H_2O)_2$ plane.

Magnetic Behavior. Under ambient pressure, magnetic data were obtained for **1** and **2** in the temperature region 2−300 K. Initial insights into the magnetism exhibited by these compounds came from theoretical fits (Supporting Information Figure S5) of the reciprocal magnetic susceptibility, $1/\chi$, to a Curie−Weiss law, $1/\chi = (T + \theta)/C$, where $C = (N_g^2\mu_B^2S(S + 1))/3k_B$, N = Avogadro's number, μ_B = Bohr magneton, k_B = Boltzman's constant. This led to the following parameters: g = 2.135(1) and θ = −6.3(1) K for **1** and g = 2.101(2) and θ = −38.8(3) K for **2**. The powder-averaged g factors are higher than the free electron value of 2.0032 but are typical of Cu^{2+} compounds, while the θ values indicate significant antiferromagnetic interactions between those Cu^{2+} centers, especially in the case of **2**.

Pressure-dependent magnetic data for **2** and **4** have also been measured, and those results are shown collectively in Figure 4. At ambient pressure, χ vs T for **2** shows a broad maximum at 28.4 K which steadily shifts to a higher temperature of 32.8 K at 0.84 GPa. It should be noted that a Curie tail was observed at lower temperature, which is attributed to the presence of a small amount of paramagnetic Cu^{2+} impurity. The weak signal of the sample and the large diamagnetic mass of the pressure cell limited data collections to below ~150 K, so that we could not reliably fit these data to a Curie−Weiss law to determine Landé g factors or Weiss constants under these conditions.

A more modest pressure effect on the magnetic susceptibility was observed for **4** (see Supporting Information Figure S6). Its structure is characterized by a 2D rectangular lattice made up of coordinate covalent Cu−Br_2−Cu ribbons that are cross-linked

dx.doi.org/10.1021/ic201924q | Inorg. Chem. 2012, 51, 2121−2129

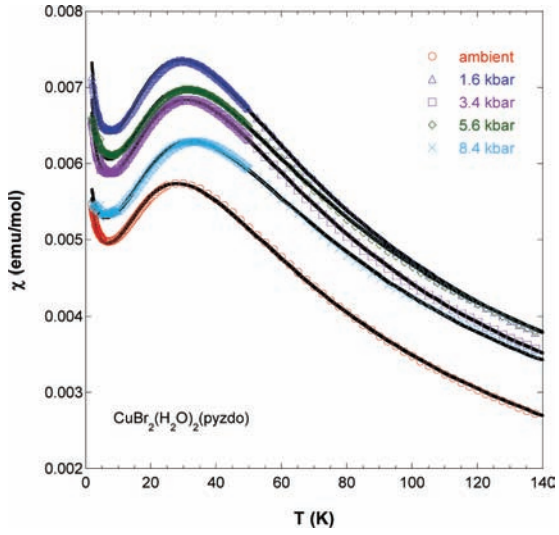

Figure 4. Magnetic susceptibility of **2** as a function of pressure. Solid lines represent theoretical fits to the data as described in the text.

by pyrazine linkages. Predictably, the additional exchange pathway offered by Cu−pyz−Cu should render a more pressure-sensitive system as confirmed by the χ vs T data. At ambient pressure, the broad maximum in χ occurs at 30.7 K and increases incrementally up to 40.7 K with application of 1.13 GPa. The peak becomes progressively more broadened as the pressure increases, which suggests an increase in the strength of the exchange interaction. Understandably, the polarizable Br ions should be quite sensitive to an external pressure, while the same effect is not apparent from the zJ' parameters given in Table 3.

The ambient and pressure-dependent magnetic susceptibility data for **2** and **4** were least-squares fitted to a Heisenberg 1D uniform antiferromagnetic chain model for $S = 1/2$[49,50] (Figures 4 and S6, Supporting Information). To adequately describe the entirety of each data set, we also incorporated a Curie component in the fit to compensate for any paramagnetic impurity (up to ∼1%) in the sample. In each case, excellent agreement was achieved using this model which is fully consistent with our density functional analysis. Use of the 1D chain model is also justified by the observation that the J_{1D} values estimated solely from the observed T_{max} are very close to those determined from the susceptibility fits (see Table 3) and from the pulsed field magnetization data (see below).[49,50] The J_{1D} value is stronger for **2** than for **1** by a factor of ∼4, which is in good agreement with the trend found in the calculated J_1 values of the previous section.

In **4**, two probable exchange pathways are present as described above; hence, a rectangular lattice model is appropriate to fit its magnetic susceptibility data.[51,52] The experimental data have been compared to the expression of a rectangular $S = 1/2$ Heisenberg antiferromagnetic model; various magnetic data parameters, including g, J, and zJ' values, are given in Table 3 for **2** and **4**. Ambient pressure magnetic susceptibility data for **3** and **4** have recently been reported elsewhere.[7] Long-range magnetic order was not readily apparent in the data shown in Figures 4 and S6, Supporting Information, for **2** and **4**. At ∼10 K, which is well below the broad maximum of **4**, a rapid decrease in χ was noted. This suggests a phase transition, but more work is necessary to find the cause for this observation.

Isothermal magnetization was measured as a function of the pulsed magnetic field. In the case of **1** and **2**, magnetization saturates at fields of 16.1 ± 0.3 and 66.7 ± 0.5 T, respectively (estimated using the extrapolation method of ref 26), with the strong upward curvature at lower fields indicative of one-dimensional magnetism[26] (Figure 5). In a Heisenberg chain, the magnetization is expected to saturate at a field $B_{sat} = -2\ k_B J_{1D}/g\mu_B$, where the dominant exchange energy J_{1D} is expressed in Kelvin.[26] Using the measured values of B_{sat} and the g factors in Table 3, we obtain $J_{1D} = -11.5 \pm 0.2$ K for **1** and $J_{1D} = -46.4 \pm 0.5$ K, for **2**, very close to the estimates derived from the susceptibility.

In the case of **3**, the saturation field is 52.0 ± 0.5 T (Figure 5). In general, for a particular geometry of exchange interaction (chain, square lattice, rectangular), the saturation field scales with a suitable sum of the characteristic exchange energies.[26] If a rectangular exchange lattice is assumed with interactions J_{1D} and J', $B_{sat} = -2\ k_B(J_{1D} + J')/g\mu_B$. Hence, the saturation field yields $J_{1D} + J = -34.5 \pm 0.5$ K.[26] In an analogous fashion to the case of **1** and **2**, the Br complex **4** saturates at a higher magnetic field, 78.2 ± 0.5 T. Using the g-factor value of **4** in Table 3, the saturation field yields $J_{1D} + J = -51.8 \pm 0.5$ K, in very good agreement with the value of 53 K estimated from the susceptibility.

In the case of **1**, the presence of interchain magnetic interactions modifies the above simple formula for the saturation field to $2J_{1D} + 4J_\perp = g\mu_B B_c$. The fact that the J_{1D} values deduced from the susceptibility and the saturation field

Table 3. Magnetic Data Fit Parameters for 1, 2, and 4

compound	P (GPa)	g	J_{1D} (K) susc/sat field	zJ' (K)	obsd T_{max} (K)	calcd $\lvert J_{1D}\rvert$ (K)[b]	ρ (%)
1[a]	ambient	2.135(1)	−11.1(1)/−11.5(2)	0	7.0	10.9	0
2[a]	ambient	2.072(2)	−45.9(1)/−46.4(5)	0	28.4	44.3	0.28
	01.6	2.054(4)	−46.7(1)	0	29.7	46.3	0.21
	03.4	2.063(2)	−48.9(1)	0	31.0	48.4	0.18
	05.6	2.019(6)	−48.9(1)	0	31.4	49.0	0.19
	08.4	2.006(1)	−51.2(1)	0	32.8	51.2	0.11
4[c]	ambient	1.973(2)	−46.9(1)	−6.1(1)	30.7	*d*	0
	03.0	1.922(2)	−52.9(1)	−5.9(1)	34.5	*d*	0
	05.2	1.939(1)	−55.6(1)	−6.0(1)	36.5	*d*	0
	08.6	1.914(1)	−60.4(1)	−5.9(1)	39.2	*d*	0
	011.3	1.883(1)	−61.7(1)	−5.8(1)	40.7	*d*	0

[a]Magnetic susceptibility data fitted to a Johnston antiferromagnetic chain model.[49] [b]$\lvert J_{1D}\rvert = 1.560 k_B T_{max}$.[49] [c]Data fitted to a spin-1/2 rectangular lattice model.[51,52] [d]It is not appropriate to calculate J_{1D} for **4** owing to the presence of significant interchain Cu−pyz−Cu interactions.

dx.doi.org/10.1021/ic201924q | Inorg. Chem. 2012, 51, 2121−2129

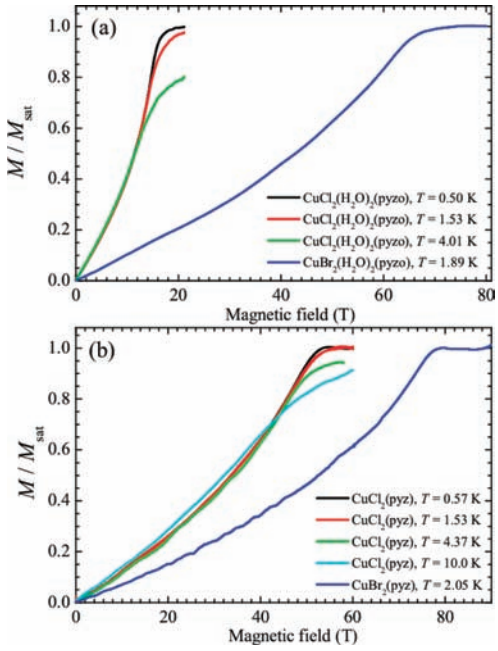

Figure 5. Isothermal magnetization of **1** and **2** (top) and **3** and **4** (bottom) as a function of magnetic field for a number of different temperatures, shown in the inset keys. High saturation fields of the Br compounds necessitated use of the Los Alamos 100 T MultiShot Magnet.

are so close in magnitude indicates negligible interchain coupling, i.e., isolated magnetic chain behavior. Applying the same methodology to **3** and using the previously reported g and $|J_{1D}|$ values of 2.12 and 14 K, respectively, we derive $|J_{\perp}| \approx 11.5$ K, indicating that the exchange is nearly isotropic.[7]

Muon-Spin Relaxation. Zero-field (ZF) μ^+SR spectra measured for **1** are shown in Figure 6. At temperatures above 1.1 K the spectra are purely relaxing and well described by a Gaussian relaxation function at early times. This behavior is typical of systems of this sort in the paramagnetic regime.[53−55] At these temperatures the Cu^{2+} electronic moments fluctuate very rapidly on the muon time scale. They are therefore motionally narrowed from the spectra, leaving the muon sensitive to the disordered quasistatic nuclear magnetic moments. This should be expected to lead to Kubo−Toyabe relaxation,[56] although slow dynamics usually alter the late time behavior, leading to the approximately Gaussian form observed.

For temperatures $T \leq 1.05$ K we observe oscillations in the muon asymmetry $A(t)$. These oscillations are characteristic of a quasi-static local magnetic field at the muon stopping site. The local field causes a coherent precession of the spins of those muons for which a component of their spin polarization lies perpendicular to this local field (expected to be 2/3 of the total spin polarization for a powder sample). We may therefore conclude that this material is magnetically ordered for $T \leq 1.05$ K. The frequency of the oscillations is given by $\nu_i = \gamma_\mu |B_i|/2\pi$, where γ_μ is the muon gyromagnetic ratio ($= 2\pi \times 135.5$ MHz T^{-1}) and B_i is the average magnitude of the local magnetic field at the ith muon site. Any distribution in magnitude of these

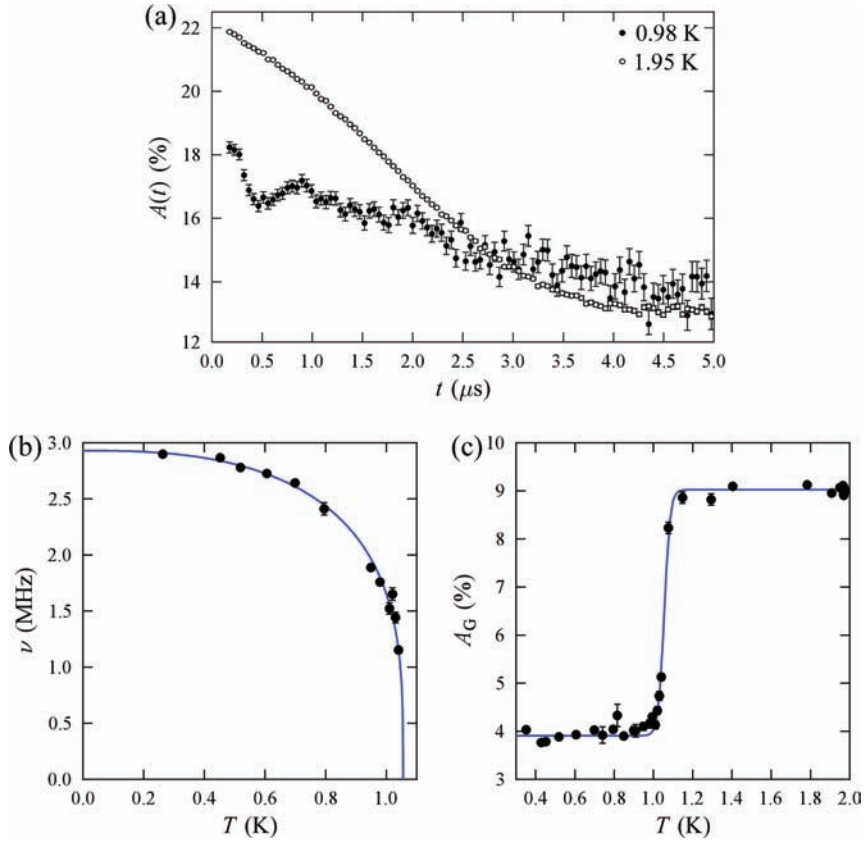

Figure 6. (a) ZF μ^+SR spectra measured for **1** above and below the magnetic transition. (b) Muon precession frequency ν as a function of temperature. Line is the result of the fit discussed in the text. (c) Magnetic transition at $T_N = 1.06$ K is most clearly seen in the sharp change of amplitude in the amplitude of the Gaussian component of the relaxation A_G at $T_N = 1.06$ K.

dx.doi.org/10.1021/ic201924q | Inorg. Chem. 2012, 51, 2121−2129

local fields will result in a relaxation of the oscillating signal, described by relaxation rates[56] λ_i. We should also expect a nonoscillating component reflecting the remaining 1/3 of muon-spin components lying parallel to the local magnetic field. In fact, the oscillations do not account for 2/3 of the total relaxing signal, and a Gaussian background signal is seen in this temperature regime. This is not unusual in ordered molecular materials and points to the existence of muon sites in regions with a large distribution of local magnetic fields.

The magnetic ordering temperature is most clearly extracted from the discontinuous change in the amplitude of the Gaussian component of the signal seen at T_N. This is shown in Figure 6c, where we see a step-like transition at $T_N = 1.06(1)$ K. The precession frequency is an effective magnetic order parameter for this system, whose behavior may be parametrized through fitting to the phenomenological function

$$\nu(T) = \nu(0)[1 - (T/T_N)^{\alpha}]^{\beta} \quad (3)$$

allowing us to extract parameters $\alpha = 2.7$ and $\beta = 0.28(1)$ describing the magnetic transition.

The ZF μ^+SR spectra measured on **2** are shown in Figure 7a. Again, the high-temperature ($T > 1$ K) spectra have a Gaussian form as in the case of **1**. The spectra change their form below $T \approx 1$ K and become more exponential in character. Exponential relaxation is often the result of dynamic fluctuations of the local magnetic field at the muon site.[56] The fact that there is no change in the apparent baseline of the relaxation strongly suggests that this is not a crossover to a static magnetic state.

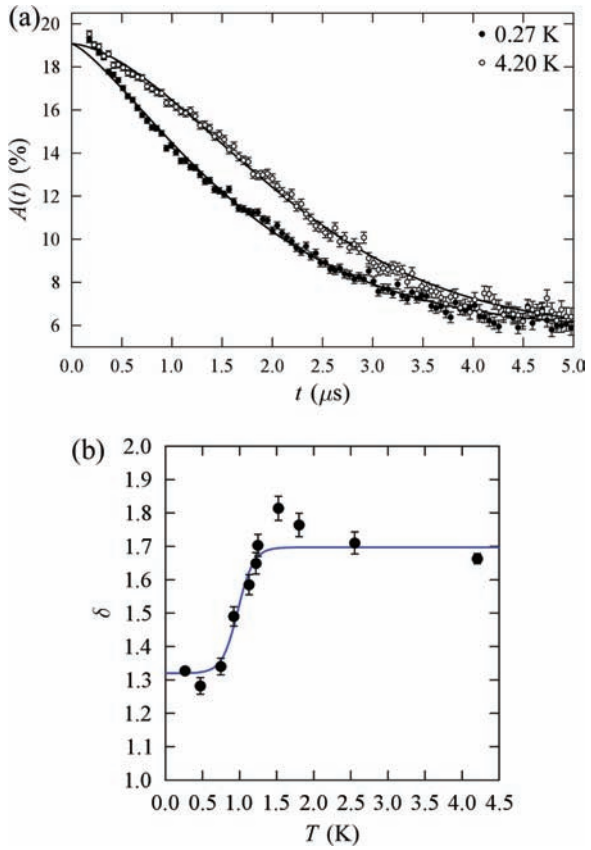

Figure 7. (a) ZF μ^+SR spectra measured for **2** showing a shape change around 1 K. (b) Temperature of the δ parameter (see main text). Line is a guide to the eye.

The crossover probably results from the fluctuations of the electronic moments on the Cu^{2+} ions slowing to a regime where they are within the muon time window. In order to parametrize the crossover the spectra were fitted to a stretched exponential function $A(t) = A_0e^{-(\lambda t)^{\delta}} + A_{bg}$, where the final term accounts for those muons which stop in the sample mount or cryostat tails. The evolution of the parameter δ is shown in Figure 2b, where we see that quite a sharp crossover takes place at 0.98 K.

It remains unclear whether the observed crossover in **2** is the consequence of some form of magnetic ordering which takes place around 1 K or to the fact that such a state occurs at a lower temperature than $T = 0.26$ K (the minimum reached in our measurements).

In the case of muon measurements on $Cu(NO_3)_2(pyz)$, for example,[53] a crossover between high-temperature Gaussian behavior and exponential relaxation, similar to the one reported here, was observed in the region close to $T \approx 2T_N$. This might suggest that **2** undergoes a transition to static magnetic order at very low temperature. Whatever the case, it is puzzling that the low-temperature magnetic behavior that we probe with μ^+SR should be so different for these two materials.

4. CONCLUSIONS

In summary, we described the crystallization of two new $Cu(pyzO)(H_2O)_2X_2$ coordination polymers. Their crystal structures contain Cu^{2+} ions linked into chains through bidentate pyzO ligands. These chains are linked into a 3D network through OH···O hydrogen bonds between the water ligands and the pyzO oxygen atoms and through halogen-bonding Cu−X···X−Cu contacts. We found that the dominant spin exchange involves supersuperexchange through the halogen-bonded Cu−X···X−Cu structure with the bromide analog exhibiting considerably (approximately four times) stronger magnetic coupling than the chloride analog. Use of the 1D chain model is also justified by the observation that the J_{1D} values estimated solely from the observed T_{max} are very close to those determined from the susceptibility fits (see Table 3) and from the pulsed field magnetization data. In the case of $CuBr_2(pyzO)(H_2O)_2$, application of hydrostatic pressure results most directly in a contraction of the hydrogen-bonded chains, while for $CuBr_2(pyz)$ the dominant compression is along the −Cu−Br_2−Cu− direction. We suggest that the pyzO ligand provides a versatile new molecular building block for construction of magnetic coordination polymers, while halogen bonding provides directional contacts that can effectively be used to design new materials with significant supersuperexchange.

■ ASSOCIATED CONTENT

Supporting Information

X-ray crystallographic details, including selected bond lengths and angles, in CIF format; X-ray powder diffraction data as a function of pressure for **4**, diagrams of possible spin exchange paths, plots of magnetic susceptibility for **4** as a function of pressure, and plots of the thermogravimetric and infrared data. This material is available free of charge via the Internet at http://pubs.acs.org.

■ AUTHOR INFORMATION

Corresponding Author

*Phone: (630) 252-3588. E-mail: JASchlueter@anl.gov.

Present Address
[▽]Department of Physics, Durham University, South Road, Durham, DH1 3LE, United Kingdom.

■ ACKNOWLEDGMENTS

Work was supported by UChicago Argonne, LLC, Operator of Argonne National Laboratory ("Argonne"). Argonne, a U.S. Department of Energy Office of Science laboratory, is operated under contract no. DE-AC02-06CH11357. Work at EWU was supported by the National Science Foundation (NSF) under grant DMR-1005825. M.H.W. thanks the U.S. Department of Energy for the financial support (grant no. DE-FG02-86ER45259) and computer resources at the NERSC Center and the HPC Center of NCSU. Work at Los Alamos was supported by the U.S. Department of Energy (DoE), NSF, and State of Florida and by the DoE BES program "Science in 100 T". Muon studies were carried out at the ISIS Facility, Rutherford Appleton Laboratory, U.K., and we are grateful to STFC (U.K.) for the provision of beamtime. This work was supported by EPSRC (U.K.).

■ REFERENCES

(1) Fourmigue, M.; Batail, P. *Chem. Rev.* **2004**, *104*, 5379−5418.
(2) Fourmigue, M. In *Halogen Bonding Fundamentals and Applications*; Metrangolo, P., Resnati, G., Eds.; Structure and Bonding; Springer-Verlag: Berlin, 2008; Vol. *128*, pp 181−207.
(3) Butcher, R. T. N.; Juan, J.; Ribas-Arino, J.; Sandvik, A. W.; Turnball, M. M.; Landee, C. P.; Wells, B. M.; Awwadi, F. F. *Chem. Commun.* **2009**, 1359−1361.
(4) Pickardt, J.; Staub, B. *Z. Naturforsch.* **1997**, *52B*, 1456−1460.
(5) Fetzer, T.; Lentz, A.; Debaerdemaeder, T. *Z. Naturforsch.* **1989**, *44B*, 553−556.
(6) Lancaster, T.; Blundell, S. J.; Pratt, F. L.; Brooks, M. L.; Manson, J. L.; Brechin, E. K.; Cadiou, C.; Low, D.; McInnes, E. J. L.; Winpenny, R. E. P. *J. Phys.: Condens. Matter* **2004**, *16*, S4563−S4582.
(7) Butcher, R. T.; Landee, C. P.; Turnball, M. M.; Xiao, F. *Inorg. Chim. Acta* **2008**, *361*, 3654−3658.
(8) Ma, B.-Q.; Sun, H.-L.; Gao, S.; Su, G. *Chem. Mater.* **2001**, *13*, 1946−1948.
(9) Sun, H.-L.; Ma, B.-Q.; Gao, S.; Su, G. *Chem. Commun.* **2001**, 2586−2587.
(10) Sun, H. L.; Gao, S.; Ma, B. Q.; Su, G. *Inorg. Chem.* **2003**, *42*, 5399−5404.
(11) Sun, H.-L.; Gao, S.; Ma, B.-Q.; Chang, F.; Fu, W.-F. *Microporous Mesoporous Mater.* **2004**, *73*, 89−95.
(12) Shi, J.-M.; Xu, H.-Y.; Zhang, F.-X.; Wu, C.-J.; Lian-Dong, L. *Chinese J. Struct. Chem.* **2007**, *26*, 214−218.
(13) Kaneko, W.; Mito, M.; Kitagawa, S.; Ohba, M. *Chem.—Eur. J.* **2008**, *14*, 3481−3489.
(14) Madea, T.; Mito, M.; Deguchi, H.; Takagi, S.; Kaneko, W.; Ohba, M.; Okawa, H. *Polyhedron* **2005**, *24*, 2497−2500.
(15) Nuttall, C. J.; Takenobu, T.; Iwasa, Y.; Kurmoo, M. *Mol. Cryst. Liq. Cryst.* **2000**, *343*, 227−234.
(16) Awaga, K.; Sekine, T.; Okawa, M.; Fujita, W.; Holmes, S. M.; Girolami, G. S. *Chem. Phys. Lett.* **1998**, *293*, 352−356.
(17) Salah, M. B.; Vilminot, S.; Andre, G.; Richard-Plouet, M.; Mhiri, T.; Takagi, S.; Kurmoo, M. *J. Am. Chem. Soc.* **2006**, *128*, 7972−7981.
(18) Laukhin, V.; Martinez, B.; Fontcuberta, J.; Amabilino, D. B.; Minguet, M.; Veciana, J. *J. Phys. Chem. B* **2004**, *108*, 18441−18445.
(19) Mascarenhas, F.; Falk, K.; Klavins, P.; Schilling, J. S.; Tomkowicz, Z.; Haase, W. *J. Magn. Magn. Mater.* **2001**, *231*, 172−178.
(20) Larionova, J.; Kahn, O.; Bartolome, J.; Burriel, R.; Castro, M.; Ksenofontov, V.; Gutlich, P. *Chem. Mater.* **1999**, *11*, 3400−3405.
(21) Shum, W. W.; Her, J.-H.; Stephens, P. W.; Lee, Y.; Miller, J. S. *Adv. Mater.* **2007**, *19*, 2910−2913.
(22) Sheldrick, G. M. *SADABS*, Version 2.03a; Bruker AXS, Inc.: Madison, WI, 2001.
(23) Sheldrick, G. M. *SHELXTL*, Version 6.12; Bruker AXS Inc.: Madison, WI, 2001.
(24) Le Bail, A.; Duroy, H.; Fourquet, J. L. *Mater. Res. Bull.* **1988**, *23*, 447.
(25) Rodriguez-Carvajal, J. *Physica B (Amsterdam)* **1993**, *192*, 55−69.
(26) Goddard, P. A.; Singleton, J.; Sengupta, P.; McDonald, R. D.; Lancaster, T.; Blundell, S. J.; Pratt, F. L.; Cox, S.; Harrison, N.; Manson, J. L.; Southerland, H. I.; Schlueter, J. A. *New J. Phys.* **2008**, *10*, 083025.
(27) Blundell, S. J. *Contemp. Phys.* **1999**, *40*, 175−192.
(28) Kresse, G.; Hafner, J. *Phys. Rev. B* **1993**, *47*, 558−561.
(29) Kresse, G.; Furthmuller, J. *Comput. Mater. Sci.* **1996**, *6*, 15.
(30) Kresse, G.; Furthmuller, J. *Phys. Rev. B* **1996**, *54*, 11169−11186.
(31) Perdew, J. P.; Burke, K.; Ernzerhof, M. *Phys. Rev. Lett.* **1996**, *77*, 3865−3868.
(32) Dudarev, S. L.; Bottom, G. A.; Savrasov, S. Y.; Humphreys, C. J.; Sutton, A. P. *Phys. Rev. B* **1998**, *57*, 1505−1509.
(33) Nather, C.; Kowallik, P.; Jess, I. *Acta Crystallogr., Sect. E* **2002**, *58*, o1253−o1254.
(34) Babu, N. J.; Nangia, A. *CrystEngComm* **2007**, *9*, 980−983.
(35) Brese, N. E.; O'Keeffe, M. *Acta Crystallogr., Sect. B* **1991**, *47*, 192−197.
(36) Brown, I. D.; Altermatt, D. *Acta Crystallogr., Sect. B* **1985**, *41*, 244−247.
(37) Halder, G. J.; Chapman, K. W.; Schlueter, J. A.; Manson, J. L. *Angew. Chem., Int. Ed. Engl.* **2011**, *50*, 419−421.
(38) Koelsch, C. F.; Gumprecht, W. H. *J. Org. Chem.* **1958**, 1603−1606.
(39) Klein, B.; Berkowitz, J. *J. Am. Chem. Soc.* **1959**, *81*, 5160−5166.
(40) Kakiuti, Y.; Kida, S.; Quagliano, J. V. *Spectrochim. Acta* **1963**, *19*, 201−211.
(41) Kida, S.; Quagliano, J. V.; Walmsley, J. A.; Tyree, S. Y. *Spectrochim. Acta* **1963**, *19*, 189−199.
(42) Speca, A. N.; Pytlewski, L. L.; Karayannis, N. M. *J. Inorg. Nucl. Chem.* **1973**, *35*, 4029−4039.
(43) Podgajny, R.; Pinkowicz, D.; Korzeniak, T.; Nitek, W.; Rams, M.; Sieklucka, B. *Inorg. Chem.* **2007**, *46*, 10416−10425.
(44) Whangbo, M.-H.; Koo, H.-J.; Dai, D. *J. Solid State Chem.* **2003**, *176*, 417−481.
(45) Xiang, H. J.; Lee, C.; Whangbo, M. H. *Phys. Rev. B* **2007**, *76*, 220411.
(46) Koo, H.-J.; Whangbo, M.-H. *Inorg. Chem.* **2008**, *47*, 128−133.
(47) Koo, H.-J.; Whangbo, M. H. *Inorg. Chem.* **2008**, *47*, 4779−4784.
(48) Whangbo, M. H.; Koo, H. J.; Dai, D.; Jung, D. *Inorg. Chem.* **2008**, *42*, 3898−3906.
(49) Johnson, D. C.; Kremer, R. K.; Troyer, M.; Wang, X.; Klumper, A.; Bud'ko, S. L.; Panchula, A. F.; Canfield, P. C. *Phys. Rev. B* **2000**, *61*, 9558−9606.
(50) Klumper, A.; Johnston, D. C. *Phys. Rev. Lett.* **2000**, *84*, 4701−4704.
(51) Manson, J. L.; Lancaster, T.; Schlueter, J. A.; Blundell, S. J.; Brooks, M. L.; Pratt, F. L.; Nygren, C. L.; Koo, H.-J.; Dai, D.; Whangbo, M.-H. *Inorg. Chem.* **2007**, *46*, 213−220.
(52) Keith, B. C.; Landee, C. P.; Valleau, T.; Turnbull, M. M.; Harrison, N. *Phys. Rev. B* **2011**, *84*, 104442. Keith, B. C.; Landee, C. P.; Valleau, T.; Turnbull, M. M.; Harrison, N. *Phys. Rev. B* **2011**, *84*, 229901.
(53) Lancaster, T.; Blundell, S. J.; Brooks, M. L.; Baker, P. J.; Pratt, F. L.; Manson, J. L.; Landee, C. P.; Baines, C. *Phys. Rev. B* **2006**, *73*, 020410.
(54) Lancaster, T.; Blundell, S. J.; Brooks, M. L.; Baker, P. J.; Pratt, F. L.; Manson, J. L.; Banes, C. *Phys. Rev. B* **2006**, *73*, 172403.
(55) Lancaster, T.; et al. *Phys. Rev. B* **2007**, *75*, 094421.
(56) Hayano, R. S.; Uemura, Y. J.; Imazato, J.; Nishida, N.; Yamazaki, T.; Kubo, R. *Phys. Rev. B* **1979**, *20*, 850−859.
(57) Turnbull, M. M.; Landee, C. P.; Wells, B. M. *Coord. Chem. Rev.* **2005**, *249*, 2567−2476.